Applied Surface Science 692 (2025) 162712

Contents lists available at ScienceDirect

Applied Surface Science

journal homepage: www.elsevier.com/locate/apsusc

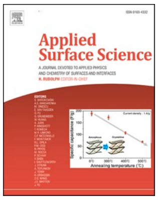

Full Length Article

Structural Insights and hydrogen retention in amorphous and crystalline tungsten oxide films

Janez Zavašnik [a,c,*], Vasyl Shvalya [a,b], Kristof Kremer [d], Thomas Schwarz-Selinger [d], Wolfgang Jacob [d]

[a] Jožef Stefan Institute, Jamova cesta 39, 1000 Ljubljana, Slovenia
[b] Jožef Stefan International Postgraduate School, Jamova cesta 39, 1000 Ljubljana, Slovenia
[c] Max-Planck-Institut für Nachhaltige Materialien, Max-Planck-Str. 1 40237 Düsseldorf, Germany
[d] Max-Planck-Institut für Plasmaphysik, Boltzmannstraße 2, 85748 Garching bei München, Germany

ARTICLE INFO

Keywords:
Tungsten oxide
Thin films
Hydrogen isotopes
Deuterium uptake
Crystal structure

ABSTRACT

We investigated structural characteristics of and hydrogen isotope interactions with thermally and electrochemically synthesized tungsten oxide (W-oxide) thin films ($\leq$50 nm). Specifically, we assessed whether electrochemically synthesized W-oxide could serve as a suitable proxy for thermally grown films in hydrogen interaction studies. The W-oxide thin films were exposed to low-energetic atomic deuterium (D) to explore the hydrogen uptake, retention, and intercalation effects of the W-oxide structure. The W-oxides were characterized using grazing incidence X-ray diffraction (GI-XRD), scanning and transmission electron microscopy (SEM, TEM), Raman spectroscopy, and Fourier-transform infrared spectroscopy (FTIR) before and after deuterium exposure. The thermally grown W-oxides are crystalline, composed of orthorhombic WO_3, while the electrochemically grown W-oxides are amorphous with nanocrystalline domains. Deuterium retention studies revealed that the electrochemically grown W-oxides show higher initial D retention compared with their thermally grown counterparts and lower D release over time during storage, suggesting stronger D binding within the amorphous matrix. Using ion beam analysis, we quantified the deuterium retention and examined the depth-resolved reduction of the oxide within the films following deuterium exposure.

1. Introduction

Tungsten (W) forms multiple oxide phases, which are a promising class of transition metal oxide semiconducting functional materials used in catalysis [1], as photoelectrodes [2], electrochromic devices [3], chemical sensors [4], and energy storage [5]. Upon uptake of hydrogen (H), the W-oxide changes its optical and electrical properties, especially when applied in nano-meter scale thin films or nanostructured materials [4]. For these applications, the nature of the hydrogen interaction with W-oxide thin film is crucial, as it dictates the type of bonding, the speed of its uptake and release, and the physical effect originating from interaction. Furthermore, W-oxide thin films can also act as a hydrogen permeation barrier, an effect studied mostly in the scope of hydrogen-isotope permeation in plasma-facing W components of a future fusion reactor [6–8]. The hydrogen permeation properties in the fusion context were considered initially from the viewpoint of possible vacuum failure, as any ingress of oxygen into the vacuum vessel and its reaction with heated W will lead to formation of W-oxide thin films. Such in-situ formed W-oxide layers will act as a barrier preventing the outgassing of the hydrogen isotopes from the bulk W, and also as a trap which can chemically bond the hydrogen and its isotopes. [6,7,9,10].

In a recent study of hydrogen transport from bulk tungsten through a thin tungsten oxide (W-oxide) surface layer, electrochemically synthesized W-oxide was used as a proxy for thermally produced oxide thin films, primarily due to its ease of production, and the precise control over the film thickness [7]. Hence, one of the main objectives of our research was to explore the interactions of hydrogen isotopes with differently prepared W-oxide films, and to assess whether their interactions are comparable. The behaviour and performance of W-oxides are closely related to the degree of its crystallization [3,11]. Most W-oxide applications consider using amorphous W-oxide, which can be reliably produced as thin films with a uniform thickness or in nanostructured form by electro-chemical oxidation, sputter deposition, sol–gel deposition, chemical vapour deposition or various other methods

---

* Corresponding author.
E-mail address: janez.zavasnik@ijs.si (J. Zavašnik).

https://doi.org/10.1016/j.apsusc.2025.162712
Received 12 December 2024; Received in revised form 8 February 2025; Accepted 15 February 2025

[4]. In sensorics, the amorphous W-oxide is preferred due to the higher surface area and faster detection/colouration speed compared with crystalline W-oxide. However, in some applications, e.g. oxides for solar cell materials, (nano-)crystalline W-oxide phases have superior performance [12,13]. Such crystalline W-oxide phases are produced by thermal oxidation of tungsten in an oxygen-containing atmosphere, or even by annealing and recrystallization of amorphous oxides [14]. The crystalline W-oxide films obtained by thermal oxidation are known to result in variable thickness depending on the crystal orientation of the underlying W grains [15]. Such W-oxide thickness variation presents a significant obstacle to improving the functional properties of the thin film, as well as uniform response to H exposure [16]. This drawback can be addressed by thermal annealing of electrochemically-produced amorphous W oxide of uniform thickness, which recrystallize into a nanocrystalline film with improved thickness uniformity [12,17].

The structural difference in amorphous and crystalline tungsten oxides can also have significant impact on functional properties of the W-oxide film, and on their response to hydrogen exposure. Up to now, most studies are concerned with specific W-oxide applications and focus on changes in the functional properties of the oxide films (e.g., light absorption, resistivity, and chemical yield) and their cyclic stability [18,19]. For fundamental insight, we investigated thermally and electrochemically grown W-oxide films with a comparable thickness of 50 nm, grown on polycrystalline W. We analysed the phase composition and crystallinity of both oxides before and after exposure to low-energy atomic deuterium (D) using Raman spectroscopy, optical microscopy (OM), scanning electron microscopy (SEM), Fourier-transform infrared spectroscopy (FTIR), grazing incidence X-ray diffraction (GI-XRD), and transmission electron microscopy (TEM). With ion beam analysis, we determined the D retention and the depth-resolved oxide concentrations within the films before and after D exposure. Specifically, we considered changes in the W-oxide structure during the intercalation of hydrogen and quantified the hydrogen isotope concentration within the oxide, as we assume significant differences in the hydrogen uptake and retention, as well as in the chemical stability (reduction) of different structural types of W-oxides.

2. Materials and methods

2.1. Bulk W sample preparation

As a bulk substrate, we used 15 × 12 mm plates of well-characterised hot-rolled polycrystalline W metal (purity 99.97 wt%, Plansee SE, Austria) [20]. The test coupons were grinded and electropolished to a mirror finish, according to the metallographic sample preparation process [21]. After polishing, the W test coupons were annealed at 2000 K for 5 min in ultra-high vacuum.

2.2. Oxidation of W test coupons

Two sets of samples were prepared, and the W test coupons were oxidized *thermally* and *electro-chemically* to a projected oxide film thickness of 50 nm.

Thermal oxidation of W test coupons was done in a vacuum furnace. To minimize contaminations, the chamber was evacuated to a base pressure of 10^{-3} Pa and purged with dry argon (purity 99.99 %). The oxidation was performed at atmospheric pressure in a mix of 20 % dry oxygen and 80 % dry argon at 600 K for of 36 h [6,22,23]. After oxidation, the samples have a dark blue colour. In the following, the thermally grown oxide films are referred to as *"T-oxides"*.

Electrochemical oxidation of W test coupons was performed as described in [7,24] in an aqueous solution of 0.4 mol/dm^3 potassium nitrate (KNO) and 0.04 mol/dm^3 nitric acid (HNO_3) at room temperature (300 K). The W sample served as an anode, and two W sheets served as a cathode. The final W-oxide film thickness was adjusted by the applied voltage of 27.3 V. In the process, the thickness of the oxide film is self-regulating and the oxidation stops when the isolating oxide film is thick enough to prevent electric current flow. In the following, the electro-chemically grown oxide films are referred to as *"EC-oxides"*.

After oxidation and before the D exposure experiments, samples were split into 4 parts to ensure accurate material characterisation and cross-correlation of the results.

2.3. Material characterisation methods

The morphology and characteristic colours of the samples were assessed by optical microscope (OM, Imager.Z1m, Carl Zeiss Microscopy GmbH) in reflective mode using RL Hal polarized light fixed at 3200 K. The micrographs were recorded by a CCD camera (AxioCam HRc, Carl Zeiss GmbH) directly coupled with the optical microscope.

The crystal structure and phase composition of the thin oxide films were analysed by grazing incidence X-ray diffraction (GI-XRD, EMPYREAN, Malvern Panalytical plc), utilising K-α radiation (1.5406 Å) from a Cu anode excited at 45 kV and 40 mA. Diffractions were collected in reflection mode, continuous 2θ scan, with 4 mm fixed mask monochromator and collimator (0.27°), with 0.01 step size and 0.05 s readout period at 2.2° take-off angle.

The analysis of surface morphology and site-specific cross-sections were made by dual-beam Scanning Electron Microscope – Focus Ion Beam with a Ga-ion source (SEM-FIB, Helios NanoLab 650i, FEI Inc.). The surface of the sample was in-chamber protected by Pt deposit, and then cut by Ga-ions at 20 kV 100 pA. The features were visualised by secondary electrons recorded by Everhart–Thornley detector at 15 kV and 0.80 nA. The phase composition and crystal structure of the nanoscale thin films were analysed by transmission electron microscope (TEM, JEM-2100, JEOL Inc.), operating at 200 kV. The cross-section samples were prepared by a combination of mechanical thinning and Ar ion etching [25].

An inelastic photon scattering study was conducted by confocal μ-Raman spectrometer collecting a signal in back-scatter geometry (NTegra Spectra II, NT-MDT LLC) using He-Ne laser operating at $\lambda = 633$ nm. A 20 × objective lens with a numerical aperture of 0.40 was used for laser-beam control.

The superficial functional groups were analysed by Fourier transform infrared spectroscopy – Attenuated Total Reflectance (ATR-FTIR, Spectrum Two, PerkinElmer) at room temperature, probing the range of wavelengths from 1800 cm^{-1} to 1100 cm^{-1} with a resolution of 4 cm^{-1}, accumulating 32 scans.

2.4. Deuterium exposure

W-oxide films samples were exposed to atomic deuterium in the well-characterized and temperature-controlled "PlaQ" plasma source [26,27]. In our experiment, the hydrogen isotope deuterium (D) was used instead of the naturally abundant protium (H) to allow accurate quantification of the areal density (amount) of D in the oxide film with ^{3}He nuclear reaction analysis. To ensure that only atomic D with thermal energies reaches the surface of the sample, a metal shutter between the opening of the plasma cage and the sample prevents direct plasma exposure [26]. The reason for this very gentle atomic D loading is to minimize the D-induced reduction of the W-oxide, observed in previous studies [6,22]. Further, the straightforward W-oxide loading with D_2 gas at low temperatures is not feasible as a catalyst (e.g. Pd) would be necessary to split D_2 on the sample's surface into atomic D (or H), which can uptake into the oxide [13]. All D exposure experiments were conducted at a temperature of 370 K to facilitate sufficient D uptake into the oxide, without causing thermally induced reduction of the W-oxide.

2.4.1. Deuterium areal density and depth profiles

The D areal density (amount) and the depth-dependent D concentration in the sample were assessed by nuclear reaction analysis (NRA), applying D(^{3}He, p)^{4}He and D(^{3}He, ^{4}He)p nuclear reactions [28,29] and exploiting different incident ^{3}He-ion energies to probe different depths in the sample. As the information depth is determined by the stopping power of the material and the energy of the incident ^{3}He-ions, we used energies of 500–4500 keV to probe the first 7 μm of the sample, i.e., the oxide film and the underlying bulk W metal. The uncertainty in the quantification of the total D areal density is <5 % and is dominated by the uncertainty of the cross-section [30,31]. The relative uncertainty for comparison of the D areal density between different samples is, however, determined by the statistical uncertainties (counting statistics) and the machine uncertainty (energy calibration and ion dose measurement) and is <3 %. The resulting proton and alpha spectra were deconvoluted by NRADC [29].

The depth resolution depends on the stopping power of the target materials and the incident ion energy, and is sufficient to clearly separate D in the oxide film from D located in the metallic W, but cannot resolve the D depth profile within the oxide film itself [6]. As reported in previous studies of the NRA depth-dependent D concentration measurements, D is expected solely within the oxide film and has not transitioned into the metallic W substrate [6].

2.4.2. *Oxygen areal density and depth profiles*

The O areal density was determined via the ^{16}O(^{3}He, p$_0$)^{18}F nuclear reaction at an incident ^{3}He energy of 4 MeV using cross-section data from [32]. The total uncertainty for oxygen quantification with this method is <5.6 %, and is composed of the uncertainty in the cross section (4.5 %) and statistical uncertainty (3 %), following Gaussian error propagation. In total, the uncertainty for the relative comparison of oxygen areal densities in the samples is within 3 %.

The depth-resolved concentration (depth profile) of oxygen within the W-oxide films was quantified via Rutherford backscattering spectroscopy (RBS) performed before and after exposure to atomic D, using ^{4}He ion beam at an energy of 800 keV and an incident angle of 70.5° to the surface normal. The latter enhances the geometric path through the film by a factor of three and by this improves the depth resolution. A detailed description of this method is given in [6]. The resulting uncertainty in the determination of the oxygen and W concentrations within the oxide film is <1 %. Regarding the thermally oxidized samples, it should be noted that the beam spot (1 mm^2) averages over multiple W grains (diameter of 10–50 μm), and the grain-dependent thickness distribution of the oxide film becomes relevant when interpreting the results. However, since the distribution of the grain orientation is known from electron backscatter diffraction measurements it can be fully accounted for and, thus, does not further influence the results [15].

3. Results and discussion

Microstructure and physical properties of the electrochemical and thermally grown W-oxide.

The exposed surface of the W samples shows well-defined grains with an average grain diameter of 10–50 μm. After the oxidation processes, the thermally (T) and electrochemically grown (EC) oxide have visually similar dark blue-violet colours (SI, Fig. S1). Under polarised light, both T-oxide and EC-oxide show vivid colouration that differs from the reported colour of W-oxides as a bulk material: yellow for WO_3, brown for WO_2, and blue for sub-stoichiometric WO_{3-x}, where $0 \leq x \leq 1$) [8,28]. Due to the nano-scale film thickness, the thin film on polished W substrates shows strong interference colours that depend on the refractive index and thickness of the W-oxide. For thermally (T) synthesised W-oxide, we distinguished 3 main different colour groups: blue, violet and yellow, covering individual W grains (Fig. 1 **a,c**). The electrochemically (EC) synthesised oxide has a uniform blue colour regardless of the underlying W grain orientation (Fig. 1 **b,d**).

To correlate the interference colours observed by Optical Microscopy (OM) with the actual thickness of the W-oxide film, we performed a combined OM and Focused Ion Beam – Scanning Electron Microscope (FIB-SEM) analysis at identical locations. Regions with different interference colours in OM were located with the SEM, followed by FIB cross-section cuts for thickness measurements. Additional data points were obtained by positioning the cross-sections directly over the grain boundaries. For the EC-oxide, the thickness of the W-oxide film is uniform across the entire sample, consistent with the intended value of 50 nm, with no variation over the grain boundaries (Fig. 1**f**, and corresponding cross-section 6). In contrast, for the T-oxide, the oxide thickness ranged from 25 nm (yellow regions) to 55 nm (blue regions) (Fig. 1**e**, and corresponding cross-sections 1-5). The W-oxide film

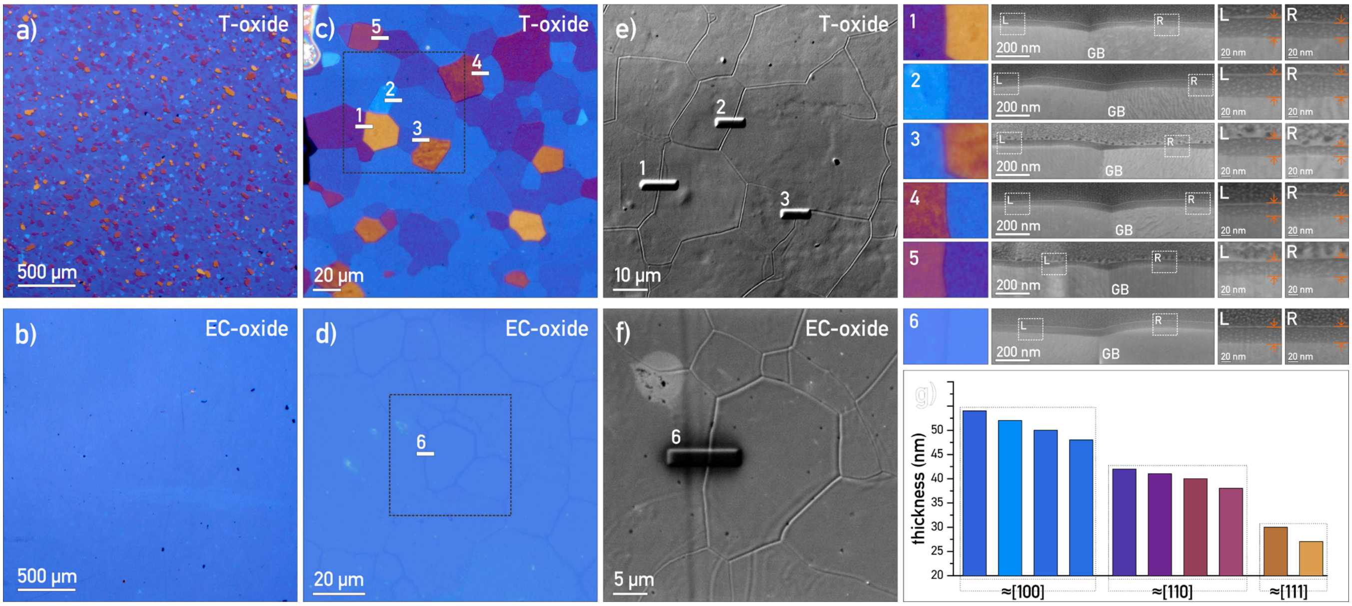

Fig. 1. Overview OM micrographs of (a) thermally oxidized (T-oxide) and (b) electrochemically oxidized (EC-oxide) samples. (c, d) Highlighted selected regions for identical location analysis. (e, f) SEM micrographs of highlighted regions, with FIB cross-section locations for thickness measurements marked, and (1–5) T-oxide OM interference colours and corresponding cross-sections, with magnified regions from left (L) and right (R) grain; the variation of the oxide film thickness is indicated by orange markers, while thickness of the EC-oxide (6) is uniform. (g) Correlation between interference colours and W-oxide thickness.

thickness was found to depend on the orientation of the underlying W grains. The W-oxide growth rate is parabolic, growing twice as fast on low-index W{100} surfaces compared with W{111} surfaces, with the oxide growth rate on W{110} being intermediate. The W grain orientation is random, with other higher-index orientations having low oxidation rates comparable with W{111} surfaces (Fig. 1**g**). These findings align well with calculated predictions [15,23]. Thus, the interference color of T-oxide layers with a thickness below 50 nm can be also used to infer the orientation of the underlying W grasins.

The crystal structure of EC-oxide and T-oxide was analysed by GI-XRD. In case of T-oxide, the recorded reflections correspond to a well-crystallised combination of triclinic WO_3 with a minor contribution of WO_2. In the case of the EC-oxide, we recorded only a broad and diffuse peak between 20 and 25 °2θ range, which is a typical response for amorphous W-oxides [33]. No further phase identification was possible (Fig. 2, and **SI,** Fig. S2).

OM and GI-XRD after the D exposure

Both oxide types were characterised by OM and GI-XRD before and after exposure to atomic D at 370 K. Due to the changes in optical properties of the oxide after the intercalation of D, information on the D uptake/intercalation can be extracted from the colour changes of the oxides after D exposure. After D exposure, the crystal structure of the T-oxide appears unchanged, but an increase of the peak at 28 °2θ can be noted, which coincides with WO_3 (PDF #20–1324) and hydrated W-oxide ($H_{0.23}WO_3$, PDF #42–1261). Immediately after exposure, the hue of both oxides changed to yellow and slowly degraded upon exposure to humidity (Supplementary Information File, Fig. S1). The initial colour shift to yellow we attribute to the formation of hydrated tungsten oxides due to the intercalation of deuterium. Over time, as deuterium is released and the hydration effect diminishes, the oxide reverts to its original state. This behaviour is indicative of reversible hydrogen interactions with crystalline structures, a characteristic not observed in the amorphous EC-oxide. To assess the D retention in the oxide, samples were re-analysed after 70 days. No structural differences in the W-oxides can be detected by GI-XRD. The OM images in Fig. 2 show the interference colours of the oxide films before exposure, 70 days after the D exposure, and 700 days after the exposure. After prolonged D degassing, the T-oxide does not show any significant changes. Conversely, the EC oxide still shows a vivid purple colour even after 700 days, indicating a change of optical properties due to the intercalation of D, but at the same time maintaining its homogeneity.

Deuterium depth profiling by NRA

After the D exposure, the D accumulation in the W-oxides was first analysed by NRA 7 days after the D exposure; the D depth profiles of T- and EC-oxides are summarised in Fig. 3 **a,b**. During exposure to atomic D, a significant amount of D enters both types of oxide film: amorphous EC-oxide has a slightly higher D concentration of 4.5 at.% compared with the 3.6 at.% in the well-crystalline T-oxide.

The samples were stored in vacuum, and the D depth profiles of both samples were re-measured 70 days after the D exposure to determine the D release from the oxide over time (Fig. 3 **c,d**). The D concentration in T-oxide has decreased by 92 %, from 13.5 ± 0.4 to $1.0 \pm 0.1 \times 10^{19}$ D/m^2, indicating that the D retention in the crystalline T-oxide is almost completely reversible, and that the binding energy of D in the T oxide is low enough to allow an almost complete release during storage at room temperature. On the other hand, after 70 days the EC-oxide retains the majority of D, and the D content decreased by only 18 %, from 17.5 ± 0.5 to $14.4 \pm 0.5 \times 10^{19}$ D/m^2, indicating that D is more strongly bound compared with T-oxide.

Oxygen areal density and depth profiles by ^{3}He-NRA.

Immediately after oxidation, the average oxygen areal density measured by ^{3}He-NRA of the T-oxide is $276 \pm 9 \times 10^{19}$ atoms/m^2, and for the EC-oxide is $295 \pm 9 \times 10^{19}$ atoms/m^2. This shows that the total oxygen areal density of the T and EC oxides films agree within 7 %. After exposure to atomic D, the oxygen areal density of both samples does not change within the measurement uncertainties; $282 \pm 9 \times 10^{19}$ atoms/m^2 for the T-oxide and $291 \pm 9 \times 10^{19}$ atoms/m^2 for the EC-oxide, indicating no significant amount of oxygen is removed from the W-oxides during the intercalation of D. However, ^{3}He-NRA for oxygen has no depth information and does, therefore, not allow to investigate changes after D exposure, e.g., partial surface reduction or O transport within the oxide film. For clarification, we analysed the homogeneity of O concentration by RBS-based oxygen depth profiling. The depth-dependent oxygen concentrations within the T- and EC-oxides directly after oxidation are shown in Fig. 4 **a,b**. The O content of the T-oxide is close to stoichiometric WO_3 (75 at% O and 25 at% W) throughout most of the film thickness and only the topmost 10 nm show a slight O concentration increase. Similarly, the EC-oxide shows a uniform oxygen depth profile with an average oxygen concentration of 76 at%; considering the method uncertainty of 1 at%, the measured oxygen concentration would correspond to stoichiometric WO_3, too.

The oxygen depth profiles after exposure to atomic D (Fig. 4 **c,d**)

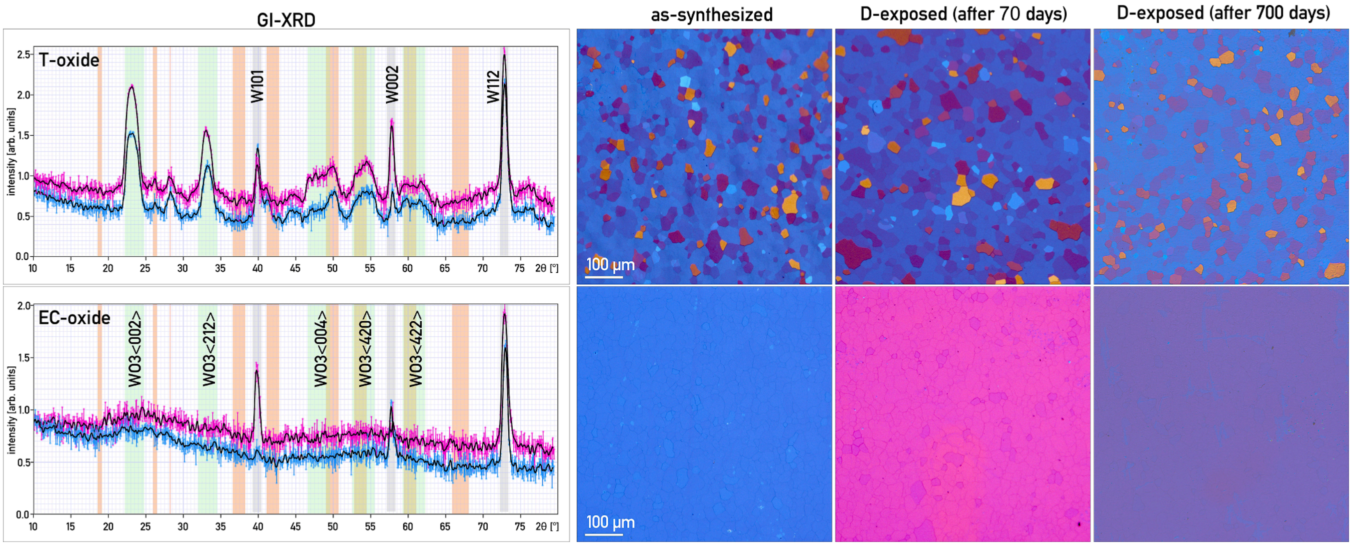

Fig. 2. Left: GI-XRD analysis of thermally oxidised (top) and electrochemically oxidised (bottom) W-oxide. The main peaks for W (grey), WO_3 (green) and WO_2 (orange) are marked as a reference. Blue is the initial scan, and purple is 180 days after the D exposure. Red vertical line marks the hydrated W oxide peak. Right: OM images showing interference colours of the oxide films before exposure, 70 days after the D exposure, and 700 days after the exposure.

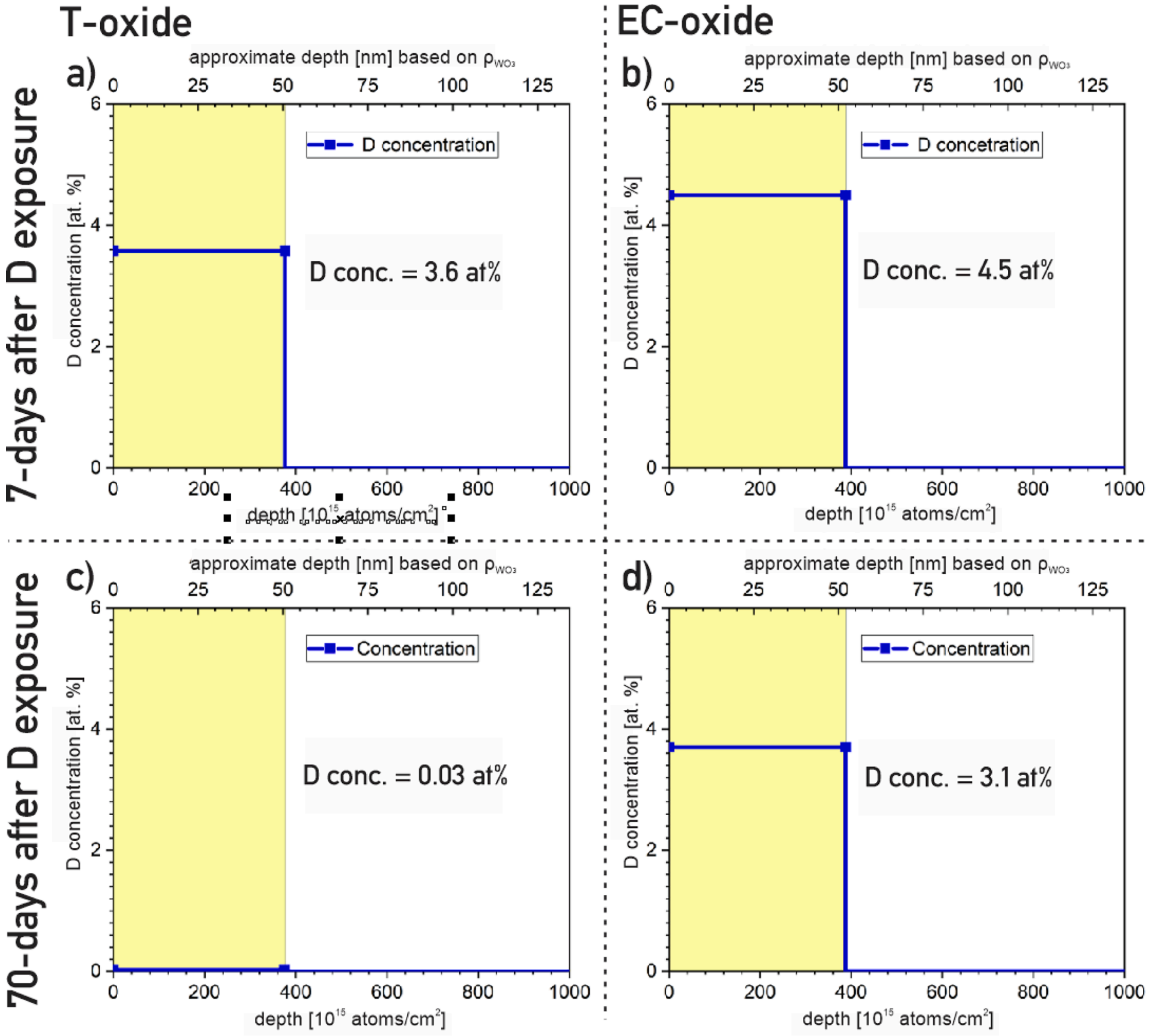

Fig. 3. Deuterium concentration as function of depth of thermally grown (left) and electrochemically grown (right) oxide. In both cases, D is only found within the surface oxide layer itself and not in the underlying metallic W. Initially, the EC-oxide has higher D retention of 4.5 at.% compared with the T oxide of 3.6 at.%. After 70 days, the D concentration decreased by 92 % in T-oxide, and by 18 % in EC-oxide.

remain identical, within the uncertainty of the method. Specifically, no W enrichment in the near-surface region of the oxide was observed, as was the case of exposure to D plasma with D ion energies of 5 eV/D [22]. As mentioned before, in the present experiment, the D has even lower energies as a shutter blocks the direct path from the plasma source to target. D can only reach the sample surface after gas phase or wall collision and has hence an energy corresponding to the gas temperature, less than ~0.1 eV. Such low D energy does obviously not cause a measurable reduction of the W-oxide. In combination with the significant D uptake of ~4 at.% observed in both W-oxides, we can conclude that the intercalation of low energetic D atoms into amorphous or nanocrystalline oxide films does not cause a measurable reduction at exposure temperatures below 370 K. The surface reduction of the W-oxide film only takes place when it is exposed to energetic D particles (≥5 eV) or exposed at higher temperatures.[34].

Crystal structure and phase composition by transmission electron microscopy

To analyse the influence of D loading on the W-oxide crystal structure, both oxides after D exposure were analysed by TEM. The sample preparation is challenging due the sensitivity of the oxide to temperature and moisture, but a combination of manual thinning and Ar-ion etching yielded satisfactory results for the observation of nano-metre oxide scales in cross-section [10]. In T-oxide, we identified a 45 nm thick crystalline oxide layer in the form of pillar-like crystals extending through the whole thickness of the oxide layer, identified as orthorhombic WO_3 (Fig. 5**a**). No orientation-dependence between W-oxide crystallites and the W substrate underneath was observed. The oxide-metal interface follows low-index crystal planes of the W substrate. The oxide thickness on the W(010) surface coincides with the predicted thickness derived from interference colours. No trace of metallic W was observed on the surface of the W-oxide. In EC-oxide, we identified a continuous 25 nm thick near-amorphous oxide layer (Fig. 5**b**), which is thinner than expected. Possible reasons are selective etching and re-deposition of W during Ar-ion milling. Inside the layer, only short-range ordered crystallite domains smaller than 2 nm were observed resembling hexagonal WO_3 and monoclinic WO_2, which corresponds to the low-intensity diffuse peaks observed in (GI-)XRD. Individual crystal domains are randomly orientated inside an amorphous W-oxide without any preference towards the W substrate. The interface is flat, suggesting continuous propagation of the oxidation. As in the case of T-oxide, also the top layer of the EC-oxide is free of any metallic W.

Raman and FTIR analyses

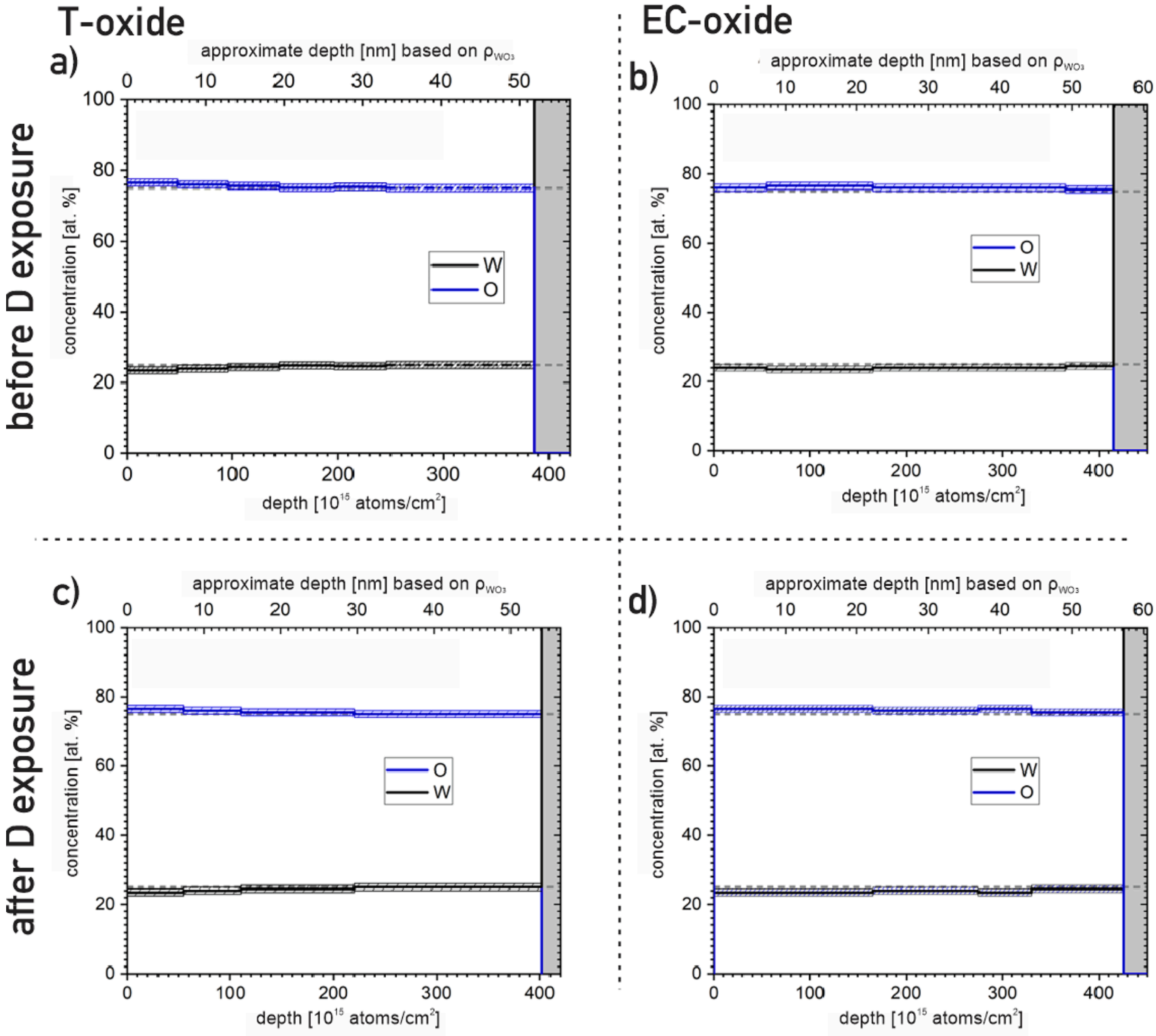

Fig. 4. Oxygen concentration as a function of depth as measured by RBS before and after atomic D exposure. (a,c) thermally grown oxide, (b,d) electrochemically grown oxide. Before D exposure, for both oxides the O concentration is close to stoichiometric WO_3 (75 at% O), with a slight O increase for the T-oxide in the near-surface region. After D exposure, the oxygen concentration in both films remains unchanged, and no surface reduction can be detected.

The μ-Raman and FTIR analyses were performed to explore possible interaction with and uptake of D into W-oxides during exposure, and to determine how the crystal structure affects the D – W-oxide interactions and how the D uptake affects the crystal structure of the W-oxide. Additionally, to clarify if reduction happens during D intercalation and to determine and compare the overall D uptake of both oxides. Both analyses were performed 7 days after D exposure.

The μ-Raman analyses were performed on as-received samples in air. For the T-oxide (Fig. 6**a**), a narrow and intense phase-defining peak (green) is located close to 807 cm^{-1} (W—O stretching vibration), indicating the presence of an orthorhombic WO_3 crystalline lattice. A set of three fitted red peaks serve as an additional indicator of orthorhombic WO_x occurrence (after [35], and Table 2 within). After deuterium uptake, there is an increased contribution of hydrated oxides (blue peaks in Fig. 6**a**,**b**). This can be interpreted as retention of deuterium by W═O and creation of W—OH/W—OD bonds within the structure [36]. Due to the D retention the contribution of the blue peak to the whole signal increases by a factor of two for this T-oxide (Fig. 6**a**,**b**). However, there is no observed influence on sample crystallinity, as concluded from the peak width. For the EC-oxide, the green peak located at 777 cm^{-1} is hardly resolved (too wide), and two additional vibrational modes placed at 696 and 660 cm^{-1} can give a hint that the dominant structure is monoclinic WO_2 [35]. Nevertheless, the width of the green peak indicates that the structure is more likely amorphous and not crystalline and involves the contribution of WO_3. After interaction with deuterium there is not only a significant change of the blue W—OH/W—OD-related Raman modes (factor 3 increase in relative contribution), but also a visible alteration of structure related to W—O vibrations is observed (blue peaks in Fig. 6**c**,**d**). Overall, the EC-oxide is more affected by deuterium uptake than the T-oxide.

Raman spectroscopy is highly dependent on structural properties and works for modes (vibrations) that induce changes in polarizability of molecules. In contrast, FTIR probes changes in dipole moments, thus being complementary to Raman. The structure-related O—W—O vibrations of the T-oxide sample undergo only slight widening after deuterium uptake (Fig. 7**a**). Additionally, in this particular case, FTIR was not able to confirm the presence of hydroxide bounds (Fig. 7**a1**). The opposite happens for the EC-oxide. In here, there is a drastic alteration (new modes occur) of O—W—O bonding environments, confirming a high structural sensitivity of the sample to the deuterium treatment (Fig. 7**b**). Moreover, complementing Raman results, FTIR reveals the presence of bending vibrations (H—O—H at 1660 cm^{-1}) in both EC-oxide samples (before and after deuterium uptake). It confirms that this sample is more favourable to create hydroxides (most probably, a

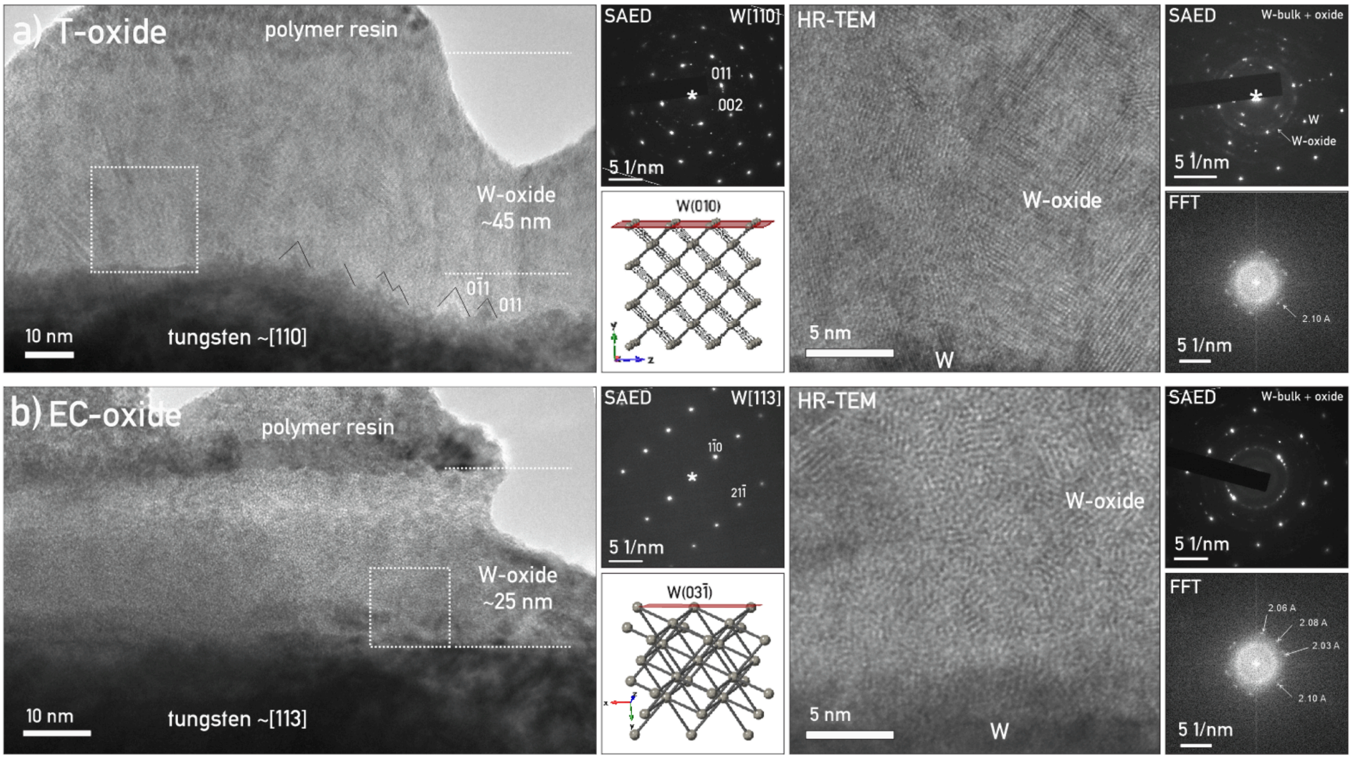

Fig. 5. From left to right: TEM micrograph of (a) thermally oxidised, and (b) electrochemically oxidised tungsten oxide, with selected area electron diffraction (SAED) from the bulk W substrate and a schematic corresponding to the crystal structure. Followed by phase contrast (HR-TEM) micrographs, and the corresponding SAED and the fast Fourier transform (FFT) from same region, with marked lattice spacing. Pillar-like T-oxide crystals correspond to orthorhombic WO_3. The crystal domains embedded in amorphous W-oxide correspond to WO_2 and WO_3.

presence of small H—O—H small hump dark green curve in Fig. 7**b1** is related to environmental humidity). A crucial observation of Fig. 7**b1** is the much more intense 1660 cm^{-1} mode and, more importantly, a new peak located at 1450 cm^{-1} (H—O—D bending motion [37]) confirming more favourable interaction of deuterium with EC-oxide than that of T-oxide.

Mechanisms of deuterium uptake and structural changes in W-oxide

Amorphous materials generally have higher ability to absorb hydrogen or deuterium than crystalline materials, which is due to a higher density of defects, a short-order arrangement of atoms, free volume, and undercoordinated sites. This mechanism has been confirmed in various metals, such as W [38] and Be [39,40], as well as in oxide system based on Zn [41], and Zr [42]. The lack of long-range periodicity in amorphous structures results in a broad distribution of energetically favourable interstitial sites, allowing easier H or D diffusion and formation of stable bonds, such as —OH or —OD groups. In contrast, crystalline phases have strictly defined lattice arrangements and the binding sites are less accessible, and the hydrogenation occurs only at limited specific defects (vacancies, grain boundaries) or requires a higher chemical potential to occupy interstitial lattice positions. Regardless of whether the oxide is amorphous or crystalline, the initial interaction of hydrogen with the surface oxygen sites leads to the formation of hydroxyl groups (—OH or —OD). However, amorphous surfaces often have more reactive oxygen sites, which allow faster and more extensive formation of hydroxyl groups. In contrast, crystalline surfaces have well-defined, lower energy terminations, resulting in fewer undercoordinated sites and, consequently, fewer nucleation points for hydroxyl layer formation, unless additional defects (vacancies, steps, kinks) are introduced externally. Consequently, the kinetics of hydrogen uptake are generally faster and more extensive in amorphous oxides. The hydroxyl or deuteroxyl layers that form on the surface of amorphous materials tend to develop more extensively compared to crystalline materials.

For the tungsten oxides investigated in this study, these general principles lead to observable differences in the Raman and FTIR spectra when interacting with deuterium (D). In the more crystalline, orthorhombic tungsten oxide (T-oxide), well-defined W═O environments favour the formation of W—OD or W—OH bonds upon deuterium exposure, but the overall lattice remains relatively intact. The long-range periodicity restricts significant structural rearrangements, such that the characteristic Raman peak at 807 cm^{-1} retains its sharp, narrow profile and FTIR reveals only a slight broadening of the O—W—O vibrations. This indicates that the deuterium is incorporated but does not significantly disturb the orthorhombic framework. In contrast, partially amorphous or disordered tungsten oxide (EC oxide) contains a higher density of defects and loosely coordinated sites that allow greater incorporation of deuterium and bond formation. Raman spectroscopy confirms an increased contribution of W—OH/W—OD-related modes, often by a factor of two or three, and also indicates more pronounced changes in W—O vibrations, suggesting significant structural reorganization. The FTIR results complement these findings, pointing to new bending vibrations (H—O—D around 1450 cm^{-1}) that demonstrate the presence of deuterium-containing groups at the material surface. In general, H—O—H bending appears at 1600–1650 cm^{-1}, H—O—D at 1400–1450 cm^{-1} and D—O—D at 1200 cm^{-1}. This shift follows the inverse square root relationship between vibrational frequency and atomic mass. In our EC-oxide spectra, we clearly see the presence of H—O—H and H—O—D, although the D—O—D peak is overlaid by a broad shoulder of the metal oxide lattice, which is influenced by deuterium uptake. While both orthorhombic and amorphous tungsten oxides can accommodate deuterium, the amorphous phase undergoes a much higher degree of structural alterations, highlighting how defects and local disorder can determine the uptake of deuterium and subsequent changes in tungsten oxide materials.

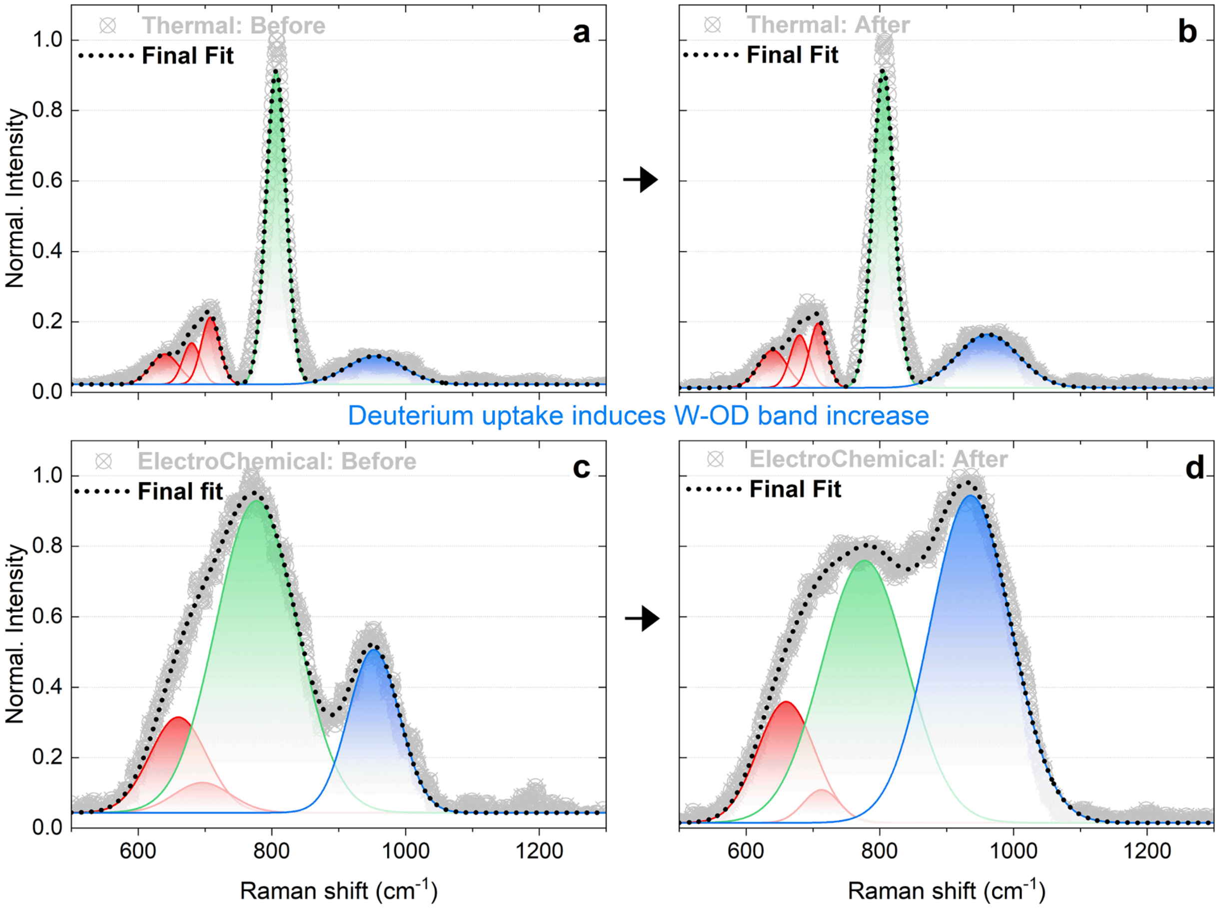

Fig. 6. Results of the μ-Raman analyses. (a,b) thermally produced oxide (T-oxide), and (c,d) electrochemically synthesised oxide (EC-oxide) before and after exposure to D atoms. No significant changes induced by D exposure in T-oxide, while in EC-oxide, the formation of deuterides is detected.

4. Conclusions

Thermally and electrochemically synthesized W-oxide films have significantly different crystal structure characteristics, which influence their interaction with low-energetic atomic hydrogen isotopes. The thermally grown W-oxide is crystalline, composed of orthorhombic WO_3, with a thickness variation dependent on the orientation of the underlying tungsten grains. In contrast, the electrochemically grown W-oxide is amorphous with uniform thickness, containing sporadic nano-scaled short-range ordered WO_2 and WO_3 crystallite domains. The structural differences are the main factor effecting deuterium retention and release. EC-oxide retains significantly more deuterium (D) than T-oxide, even after prolonged storage. We attribute this to stronger binding of D within the amorphous matrix, which is in sharp contrast with the almost complete D release observed in the crystalline T-oxide. The low binding energy in thermally grown W-oxide allows for rapid D degassing at room temperature.

Exposure to atomic deuterium at temperatures $\leq 100\,^{\circ}C$ did not cause measurable W-oxide reduction or significant alteration of the W-oxide structures, regardless of their initial crystallinity. This stability against reduction contrasts with previously reported behaviours under higher energy D plasma exposure [22,34,36]. Both W-oxides are appropriate for applications where low-energy hydrogen and its isotope exposure is prevalent.

On the one hand, the findings suggest that EC-oxide thin films may serve as more effective hydrogen permeation barrier due to their higher D retention and stability. On the other hand, T-oxide is more suitable for sensors and detectors due to short degassing time. The T-oxide can accumulate a large amount of atomic D at low temperatures ($<100\,^{\circ}C$), but degasses quickly. Contrary to that, EC-oxide can accumulate comparable amounts of atomic D, but it is chemically bonded, forming deuterides that remained stable for prolonged period.

The observed differences in hydrogen isotope retention between EC-oxide and T-oxide also dictate their different suitability for practical applications. The amorphous EC-oxide with uniform thickness has better deuterium retention, maintaining stability even after prolonged storage, making it a candidate for hydrogen permeation barriers or long-term hydrogen storage systems, where sustained retention is critical. On the other hand, T-oxide shows rapid deuterium release due to weaker binding interactions, advantageous in dynamic systems requiring rapid uptake and release, such as hydrogen sensors and detectors. The observed differences show the importance of tailoring oxide structures to specific operational requirements. Furthermore, for research purposes, the electrochemically prepared amorphous oxide is not a suitable proxy for crystalline W-oxide in terms of hydrogen interaction.

CRediT authorship contribution statement

Janez Zavašnik: Writing – review & editing, Writing – original draft, Visualization, Supervision, Methodology, Investigation, Formal analysis, Data curation. **Vasyl Shvalya:** Writing – review & editing, Visualization, Validation, Methodology, Investigation, Formal analysis, Data curation. **Kristof Kremer:** Writing – review & editing, Writing – original draft, Visualization, Investigation, Formal analysis, Data curation, Conceptualization. **Thomas Schwarz-Selinger:** Writing – review & editing, Writing – original draft, Visualization, Validation, Supervision, Resources, Project administration, Methodology, Investigation, Funding acquisition, Formal analysis, Data curation, Conceptualization.

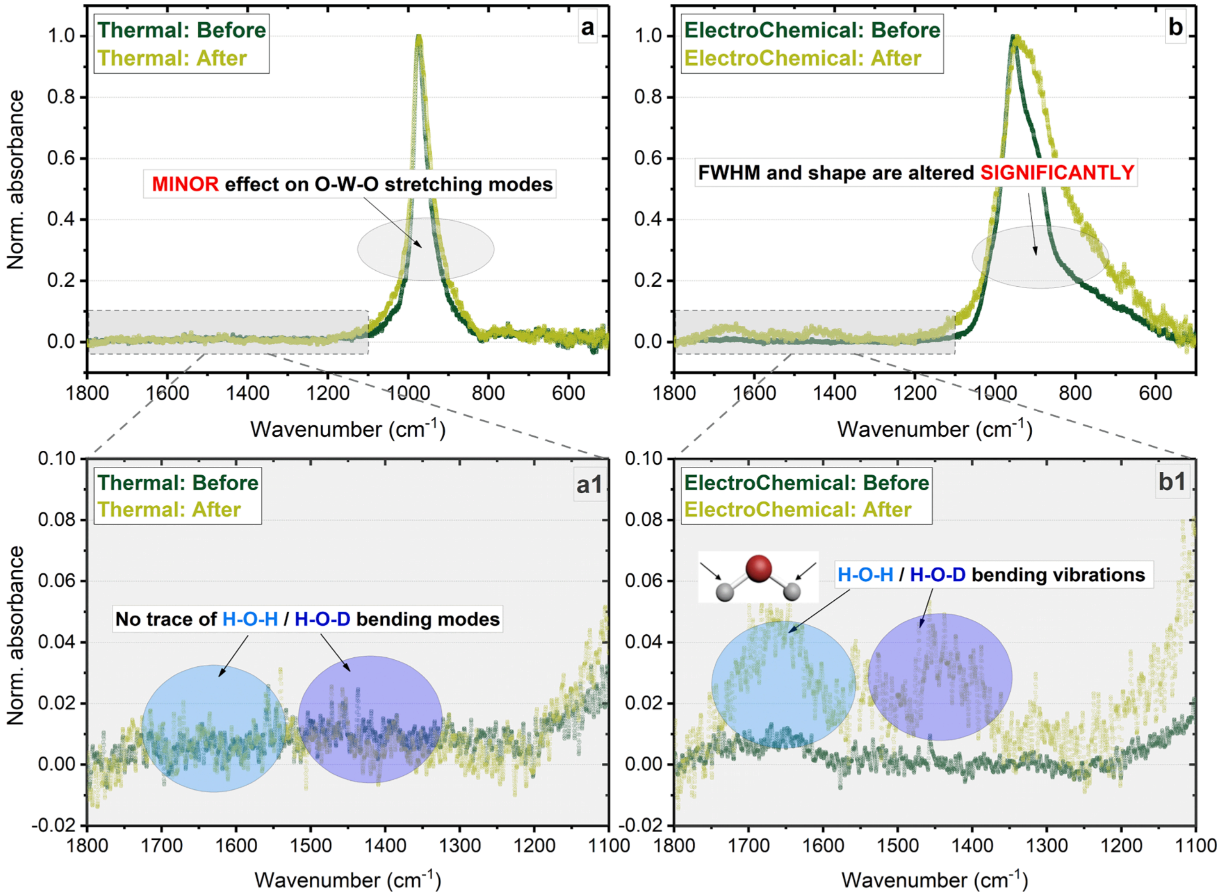

Fig. 7. Results of FTIR analysis of the (a,b) T-oxide, and (a1, b1) EC-oxide before and after exposure to D atoms.

Wolfgang Jacob: Writing – review & editing, Writing – original draft, Visualization, Validation, Supervision, Resources, Project administration, Methodology, Investigation, Funding acquisition, Formal analysis, Data curation, Conceptualization.

Declaration of competing interest

The authors declare that they have no known competing financial interests or personal relationships that could have appeared to influence the work reported in this paper.

Acknowledgements

This work has been carried out within the framework of the EUROfusion Consortium, funded by the European Union via the Euratom Research and Training Programme (Grant Agreement No 101052200 — EUROfusion). Views and opinions expressed are however those of the author(s) only and do not necessarily reflect those of the European Union or the European Commission. Neither the European Union nor the European Commission can be held responsible for them. JZ and VS acknowledge the support by Slovenian Research Agency (ARRS) program P1-0417 and project J2-4440. JZ acknowledges the support of Max-Planck- Gesellschaft via High performance materials partner group. The authors acknowledge the financial support from the European Innovation Council Pathfinder project under ThermoDust grant agreement No. 101046835.

Data availability

Data will be made available on request.

References

[1] J.B. Christian, S.P.E. Smith, M.S. Whittingham, H.D. Abruña, Tungsten based electrocatalyst for fuel cell applications, Electrochem. Commun. 9 (2007) 2128–2132, https://doi.org/10.1016/J.ELECOM.2007.06.001.

[2] S. Feng, S. Kajita, M. Higashi, A. Bieberle-Hütter, T. Yoshida, N. Ohno, Photoelectrochemical properties of plasma-induced nanostructured tungsten oxide, Appl. Surf. Sci. 580 (2022) 151979, https://doi.org/10.1016/J.APSUSC.2021.151979.

[3] H. Wang, M. Zhang, S. Yang, L. Zhao, L. Ding, Preparation and properties of electrochromic tungsten oxide film, Sol. Energy Mater. Sol. Cells 43 (1996) 345–352, https://doi.org/10.1016/0927-0248(96)00016-5.

[4] G. Lei, C. Lou, X. Liu, J. Xie, Z. Li, W. Zheng, J. Zhang, Thin films of tungsten oxide materials for advanced gas sensors, Sens. Actuators B Chem. 341 (2021) 129996, https://doi.org/10.1016/J.SNB.2021.129996.

[5] S.P. Gupta, H.H. Nishad, S.D. Chakane, S.W. Gosavi, D.J. Late, P.S. Walke, Phase transformation in tungsten oxide nanoplates as a function of post-annealing temperature and its electrochemical influence on energy storage, Nanoscale Adv. 2 (2020) 4689–4701, https://doi.org/10.1039/D0NA00423E.

[6] K. Kremer, T. Schwarz-Selinger, W. Jacob, Influence of thin tungsten oxide films on hydrogen isotope uptake and retention in tungsten – evidence for permeation barrier effect, Nucl. Mater. Energy 27 (2021) 100991, https://doi.org/10.1016/J.NME.2021.100991.

[7] K. Kremer, M. Brucker, W. Jacob, T. Schwarz-Selinger, Influence of thin surface oxide films on hydrogen isotope release from ion-irradiated tungsten, Nucl. Mater. Energy 30 (2022) 101137, https://doi.org/10.1016/J.NME.2022.101137.

[8] V. Nemanič, J. Zavašnik, V. Shvalya, M. Žumer, Hydrogen permeability of non-stoichiometric tungsten oxides, J. Nucl. Mater. 548 (2021) 152860, https://doi.org/10.1016/j.jnucmat.2021.152860.

[9] J.W. Coenen, S. Antusch, M. Aumann, W. Biel, J. Du, J. Engels, S. Heuer, A. Houben, T. Hoeschen, B. Jasper, F. Koch, J. Linke, A. Litnovsky, Y. Mao, R. Neu, G. Pintsuk, J. Riesch, M. Rasinski, J. Reiser, M. Rieth, A. Terra, B. Unterberg, T. Weber, T. Wegener, J.H. You, C. Linsmeier, Materials for DEMO and reactor applications - Boundary conditions and new concepts, in: Phys Scr, IOP Publishing, 2016 14002, https://doi.org/10.1088/0031-8949/2016/T167/014002.

[10] A. Šestan, J. Zavašnik, M.M. Kržmanc, M. Kocen, P. Jenuš, S. Novak, M. Čeh, G. Dehm, Tungsten carbide as a deoxidation agent for plasma-facing tungsten-based materials, J. Nucl. Mater. 524 (2019) 135–140, https://doi.org/10.1016/j.jnucmat.2019.06.030.

[11] G.-F. Cai, X.-L. Wang, D. Zhou, J.-H. Zhang, Q.-Q. Xiong, C.-D. Gu, J.-P. Tu, Hierarchical structure Ti-doped WO 3 film with improved electrochromism in visible-infrared region, 3 (2013) 6896. doi: 10.1039/c3ra40675j.

[12] T. Zhu, M.N. Chong, Y.W. Phuan, E.S. Chan, Electrochemically synthesized tungsten trioxide nanostructures for photoelectrochemical water splitting: influence of heat treatment on physicochemical properties, photocurrent densities and electron shuttling, Colloids Surf. A Physicochem. Eng. Asp. 484 (2015) 297–303, https://doi.org/10.1016/J.COLSURFA.2015.08.016.

[13] S.K. Deb, Opportunities and challenges in science and technology of WO3 for electrochromic and related applications, Sol. Energy Mater. Sol. Cells 92 (2008) 245–258, https://doi.org/10.1016/J.SOLMAT.2007.01.026.

[14] G.S. Ghen, W.L. Liao, S.T. Chen, W.C. Su, C.K. Lin, Effects of deposition and annealing atmospheres on phase transition of tungsten oxide films grown by ultra-high-vacuum reactive sputtering, Thin Solid Films 493 (2005) 301–306, https://doi.org/10.1016/J.TSF.2005.07.309.

[15] K. Schlueter, M. Balden, Dependence of oxidation on the surface orientation of tungsten grains, Int. J. Refract. Metals Hard Mater. 79 (2019) 102–107, https://doi.org/10.1016/J.IJRMHM.2018.11.012.

[16] K. Mašek, J. Libra, T. Skála, M. Cabala, V. Matolín, V. Cháb, K.C. Prince, SRPES investigation of tungsten oxide in different oxidation states, Surf. Sci. 600 (2006) 1624–1627, https://doi.org/10.1016/J.SUSC.2005.11.048.

[17] A. Agrawal, H. Habibi, Effect of heat treatment on the structure, composition and electrochromic properties of evaporated tungsten oxide films: I, Thin Solid Films 169 (1989) 257–270, https://doi.org/10.1016/0040-6090(89)90709-8.

[18] S. Zhou, Z. Yang, X. Feng, J. Zuo, N. Wang, K. Thummavichai, Y. Zhu, The frontier of tungsten oxide nanostructures in electronic applications, Iscience 27 (2024) 109535, https://doi.org/10.1016/J.ISCI.2024.109535.

[19] Y. Li, M. Je, J. Kim, C. Xia, S.H. Roh, W. So, H. Lee, D.H. Kim, S.M. Cho, J.W. Bae, H. Choi, J.K. Kim, Rational nanopositioning of homogeneous amorphous phase on crystalline tungsten oxide for boosting solar water oxidation, Chem. Eng. J. 438 (2022) 135532, https://doi.org/10.1016/J.CEJ.2022.135532.

[20] A. Manhard, M. Balden, S. Elgeti, Quantitative mikrostruktur- und defektdichten-Analyse polykristalliner wolfram-referenzproben nach verschiedenen wärmebehandlungen, Praktische Metallographie/Practical, Metallography 52 (2015) 437–466, https://doi.org/10.3139/147.110354/MACHINEREADABLECITATION/RIS.

[21] A. Manhard, G. Matern, M. Balden, Eine schrittweise analyse des poliervorgangs für Wolframproben, Praktische Metallographie/Practical, Metallography 50 (2013) 5–16, https://doi.org/10.3139/147.110215/MACHINEREADABLECITATION/RIS.

[22] K. Kremer, T. Schwarz-Selinger, W. Jacob, Deuterium plasma exposure of thin oxide films on tungsten - oxygen removal and deuterium uptake, Nucl. Mater. Energy 35 (2023) 101406, https://doi.org/10.1016/J.NME.2023.101406.

[23] K. Schlueter, M. Balden, T.F. da Silva, Evaluating crystal-orientation-dependent properties on polycrystalline tungsten: example oxidation, Int. J. Refract. Metals Hard Mater. 88 (2020) 105189, https://doi.org/10.1016/J.IJRMHM.2020.105189.

[24] M. McCargo, J.A. Davies, F. Brown, RANGE OF Xe133 AND Ar41 IONS OF KEV ENERGIES IN TUNGSTEN, Https://Doi.Org/10.1139/P63-120 41 (2011) 1231–1244. https://doi.org/10.1139/P63-120.

[25] A. Šestan, P. Jenuš, S.N. Krmpotič, J. Zavašnik, M. Čeh, The role of tungsten phases formation during tungsten metal powder consolidation by FAST: implications for high-temperature applications, Mater. Charact. 138 (2018) 308–314, https://doi.org/10.1016/j.matchar.2018.02.022.

[26] A. Manhard, T. Schwarz-Selinger, W. Jacob, Quantification of the deuterium ion fluxes from a plasma source, Plasma Sources Sci. Technol. 20 (2011) 015010, https://doi.org/10.1088/0963-0252/20/1/015010.

[27] M. Pandey, R. Ahuja, R. Kumar, W. Han, J. Yu, Z. Chen, Blister formation on rough and technical tungsten surfaces exposed to deuterium plasma, Nucl. Fusion 57 (2017) 126012, https://doi.org/10.1088/1741-4326/AA82C8.

[28] M. Mayer, E. Gauthier, K. Sugiyama, U. von Toussaint, Quantitative depth profiling of deuterium up to very large depths, Nucl. Instrum. Methods Phys. Res. B 267 (2009) 506–512, https://doi.org/10.1016/J.NIMB.2008.11.033.

[29] K. Schmid, U. Von Toussaint, Statistically sound evaluation of trace element depth profiles by ion beam analysis, Nucl. Instrum. Methods Phys. Res. B 281 (2012) 64–71, https://doi.org/10.1016/J.NIMB.2012.03.024.

[30] W. Möller, F. Besenbacher, A note on the 3He + D nuclear-reaction cross section, Nucl. Inst. Methods 168 (1980) 111–114, https://doi.org/10.1016/0029-554X(80)91239-2.

[31] B. Wielunska, M. Mayer, T. Schwarz-Selinger, U. Von Toussaint, J. Bauer, Cross section data for the D(3He,p)4He nuclear reaction from 0.25 to 6 MeV, Nucl. Instrum. Methods Phys. Res. B 371 (2016) 41–45, https://doi.org/10.1016/J.NIMB.2015.09.049.

[32] M. Guitart Corominas, T. Schwarz-Selinger, Experimental determination of the 16O (3He,p0)18F differential cross section, Nucl. Instrum. Methods Phys. Res. B 450 (2019) 13–18, https://doi.org/10.1016/J.NIMB.2018.05.018.

[33] M. Mazur, D. Wojcieszak, A. Wiatrowski, D. Kaczmarek, A. Lubańska, J. Domaradzki, P. Mazur, M. Kalisz, Analysis of amorphous tungsten oxide thin films deposited by magnetron sputtering for application in transparent electronics, Appl. Surf. Sci. 570 (2021) 151151, https://doi.org/10.1016/J.APSUSC.2021.151151.

[34] F. Pappalardo, L. Rayneau, C. Martin, M. Cabie, E. Salomon, T. Angot, G. Cartry, R. Bisson, M. Minissale, In-situ monitoring of tungsten oxides reduction during deuterium plasma exposure by spectroscopic ellipsometry, Nucl. Mater. Energy 41 (2024) 101751, https://doi.org/10.1016/J.NME.2024.101751.

[35] G. Fulton, A. Lunev, Probing the correlation between phase evolution and growth kinetics in the oxide layers of tungsten using Raman spectroscopy and EBSD, Corros. Sci. 162 (2020) 108221, https://doi.org/10.1016/J.CORSCI.2019.108221.

[36] M. Li, Z. Zhao, X. Fang, L. Tegg, D. Cuskelly, V.J. Keast, B. Wang, Q. Wang, Y. Zhu, Y. Addab, C. Martin, C. Pardanaud, J. Khayadjian, K. Achkasov, D. Kogut, G. Cartry, G. Giacometti, M. Cabié, J.L. Gardarein, P. Roubin, Formation of thin tungsten oxide layers: characterization and exposure to deuterium, Phys. Scr. 2016 (2016) 014036, https://doi.org/10.1088/0031-8949/T167/1/014036.

[37] K. Park, Y. Kim, K.J. Lee, Analysis of deuterated water contents using FTIR bending motion, J. Radioanal. Nucl. Chem. 322 (2019) 487–493, https://doi.org/10.1007/S10967-019-06734-Z/TABLES/3.

[38] O.V. Ogorodnikova, J. Roth, M. Mayer, Deuterium retention in tungsten in dependence of the surface conditions, J. Nucl. Mater. 313–316 (2003) 469–477, https://doi.org/10.1016/S0022-3115(02)01375-2.

[39] M. Reinelt, A. Allouche, M. Oberkofler, C. Linsmeier, Retention mechanisms and binding states of deuterium implanted into beryllium, New J. Phys. 11 (2009) 043023, https://doi.org/10.1088/1367-2630/11/4/043023.

[40] C. Pardanaud, M.I. Rusu, C. Martin, G. Giacometti, P. Roubin, Y. Ferro, A. Allouche, M. Oberkofler, M. Köppen, T. Dittmar, C. Linsmeier, Hydrogen retention in beryllium: concentration effect and nanocrystalline growth, J. Phys. Condens. Matter 27 (2015) 475401, https://doi.org/10.1088/0953-8984/27/47/475401.

[41] C.G. Van De Walle, Hydrogen as a cause of doping in Zinc Oxide, Phys. Rev. Lett. 85 (2000) 1012–1015, https://doi.org/10.1103/PhysRevLett.85.1012.

[42] B.D. Warr, M.B. Elmoselhi, S.B. Newcomb, N.S. McIntyre, A.M. Brennenstuhl, P. C. Lichtenberger, Oxide characteristics and their relationship to hydrogen uptake in Zirconium alloys, ASTM Spec. Tech. Publ. (1991) 740–756, https://doi.org/10.1520/STP25537S.